Angewandte Chemie
Eine Zeitschrift der Gesellschaft Deutscher Chemiker

Supporting Information

Repairing Nanoparticle Surface Defects

*Emanuele Marino[+], Thomas E. Kodger[+], Ryan W. Crisp, Dolf Timmerman, Katherine E. MacArthur, Marc Heggen, and Peter Schall**

anie_201705685_sm_miscellaneous_information.pdf

Author Contributions

E.M. Conceptualization: Lead; Data curation: Lead; Formal analysis: Lead; Investigation: Lead; Methodology: Lead; Writing—original draft: Lead; Writing—review & editing: Lead
T.K. Conceptualization: Equal; Investigation: Equal; Methodology: Equal; Supervision: Equal
R.C. Data curation: Equal; Formal analysis: Equal; Methodology: Equal; Supervision: Supporting; Writing—review & editing: Supporting
D.T. Investigation: Supporting; Methodology: Supporting; Writing—review & editing: Supporting
K.M. Data curation: Supporting
M.H. Investigation: Equal; Methodology: Equal; Writing—review & editing: Supporting
P.S. Conceptualization: Equal; Funding acquisition: Lead; Project administration: Lead; Resources: Lead; Supervision: Equal; Validation: Equal; Writing—review & editing: Equal.

Chemicals

1-Octadecene (ODE, 90%, Aldrich), 2,6-dimethylpyridine (DMP, ≥99%, Aldrich), 3-methylpyridine (3MP, ≥99%, Aldrich), Acetonitrile (MeCN, anhydrous 99.8%, Sigma-Aldrich), Ammonium hydroxide solution (NH_4OH, 28.0-30.0% of NH_3, Fluka), Ammonium sulfide solution ($(NH_4)_2S$, 40-48 wt.% in H2O, Fluka), Cadmium nitrate tetrahydrate (98%, Aldrich), Cadmium acetate ($(Cd(CH_3COO)_2$), >98%, Aldrich), Cadmium oxide (≥99.99%, Aldrich), Ethanol absolute (99.6%), Hexane (anhydrous 95%, Aldrich), MilliQ water (H_2O), N-methylformamide (NMF, >99.0%, TCI Europe), Oleic acid (OA, 90%, Sigma Aldrich), Pyridine (Pyr, anhydrous, 99.8%, Aldrich), Sodium myristate (>99.8%, TCI Europe), Sodium sulfide nonahydrate (≥98.0% Fluka), Sodium stannate trihydrate (95%, Aldrich), Selenium (≥99.99%, Strem Chemicals).

Synthesis of Thiostannate ligands

Na_4SnS_4 and $(NH_4)_4Sn_2S_6$ were synthesized according to literature with minor modifications.[1] Specifically when synthesizing $(NH_4)_4Sn_2S_6$ (1) we found important washing the SnS_2 thoroughly to remove excess NaCl; (2) to speed up the reaction (average time to completion was 1 hour), we sonicated the dispersion of SnS_2 powder in $(NH_4)_2S$ in water rather than stirring it. The final solution is clear and light brown – yellow and was filtered with an 800 nm MCE filter to remove unreacted SnS_2.

Synthesis of Cadmium myristate ($Cd(C_{13}H_{54}COO)_2$)

Cadmium myristate was synthesized according to Carion et al. with no modifications.[2]

Synthesis of CdSe nanoplatelets (NPs)

CdSe NPs were synthesized according to literature with minor modifications.[3] Briefly, in a three-neck flask, 510 mg of cadmium myristate and 42 mL of ODE were heated to 100 °C under vacuum for 30 minutes. The atmosphere was then switched to nitrogen for a few seconds and then back to vacuum. The procedure was repeated three times. Finally the atmosphere was switched to nitrogen. The flask was heated to 240 °C. Once the temperature had stabilized, 3 mL of a 0.15 M dispersion of selenium powder sonicated in ODE were swiftly injected using an 18 gauge needle. After 20 s of delay, 180 mg of finely ground cadmium acetate were introduced, either as powder or as dispersion in ODE (90 mg/mL). The solution was held at 240 °C for 10 min, and the temperature was then rapidly reduced by removing the heating mantle and replacing it with a water bath. At 100 °C 6 mL of OA were added. At 70 °C 45 mL of hexane were added. The mixture was then centrifuged at 4000g for 1 hour, yielding a colored supernatant (dispersion of quantum dots, QDs) and a dark precipitate (NPs). The supernatant was discarded and the precipitate was dispersed in 10 mL of hexane. Depending on the size of the NPs, 220 nm (PTFE), 450 nm (PTFE) or 800 nm (MCE) pore sized filters were used to filter the dispersion.

By keeping the same delay time (20 s) and varying the reaction time between 5 and 30 minutes NPs with the same thickness and different aspect ratios (length of NP/width of NP) can be synthesized (Figure S1). By increasing the synthesis reaction time, NPs increase in aspect ratio through growth along the [1 1 0] direction proceeding faster than

along [1 -1 0], while thickness remains constant (Figure S1). This is in agreement with the growth preference of side facets and confirms the bias for wet annealing to trigger reconstruction along the less stable [1 -1 0] axis over the [1 1 0].

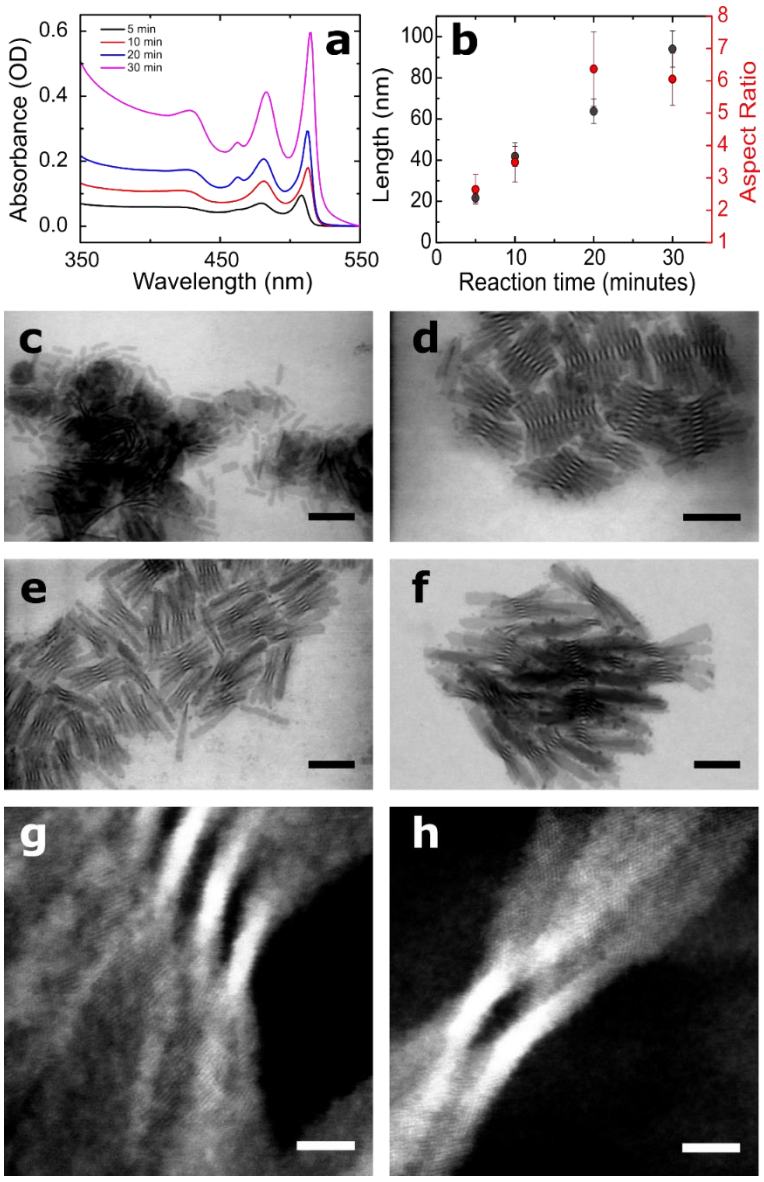

Figure S1 (a) Absorption spectra of NPs with different aspect ratios. Reaction time is indicated in the legend. (b) Measured length and aspect ratio of NPs synthesized with different reaction times. Bright field STEM images of NPs synthesized with reaction times of (c) 5 minutes, (d) 10 minutes, (e) 20 minutes, and (f) 30 minutes. High resolution HAADF STEM images of NPs synthesized with reaction times of (g) 20 minutes and (h) 30 minutes. Black scale bars indicate 50 nm, white scale bars indicate 5 nm.

Ligand exchange (LE)

Native oleate ligands were replaced with thiostannate complexes adapting the procedure from Kovalenko et al. with minor modifications.[4] 1 mL solution (0.1 M) of thiostannate salts (Na_4SnS_4 or $(NH_4)_4Sn_2S_6$) in H_2O was added to 8 mL of a polar solvent of choice (28-30% NH3 solution, pure H_2O, Pyr, 3MP, DMP or NMF). 6 mL of hexane were layered on top, resulting in a two-phase system. 1 mL stock dispersion of NPs in hexane was added to the apolar phase and the mixture was stirred vigorously until the colored dispersion of NPs had migrated from the top to the bottom phase, resulting in a colorless apolar phase. As a result of the LE, the dispersion of NPs changed color from yellow-green to orange-pink. We attribute this to an extension of the electronic wavefunction to the shell of conductive ligands. The duration of the LE process depends strongly on the choice of the polar solvent and it ranges from a few minutes (NMF), to one hour (aqueous solution of NH_4OH) to several hours (pure H_2O). The choice of the polar phase has also a strong influence on the final structural integrity of the NPs and the definition of the excitonic features in absorption (Figure S2). NMF was the only solvent to yield visually non damaged NPs; NMF also yielded the most defined absorption features in the absorption spectrum of ligand exchanged NPs. Specifically, the ligand exchange may induce structural damage as follows: the excess presence of L-type ligands may stabilize L-CdX_2 species in solution, removing part of the Cd-rich external shell. Furthermore, the electrophilic chalcogen atom may also leave the NP surface as an L-Se complex. However we hypothesize that these molecular complexes may not be very soluble in a highly polar environ-

ment and can precipitate directly on the surface of nanoplatelets, thus generating the brighter regions observed on damaged NPs after ligand exchange (Figure S3 b-d). Once the transfer was complete, the clear apolar phase was carefully removed by pipetting and the polar phase rinsed 3 times with hexane. The rinsing was done by gently tumbling the vial and not by shaking, as this may result in the formation of an emulsion that takes a long time to break. In this case, mild centrifugation (200g) effectively broke the emulsion. After rinsing, the polar phase was transferred to a centrifuge tube and MeCN was added (1:1 v/v) and the mixture vortexed and centrifuged at 4000g for 10 min. The colorless supernatant was discarded and the colored pellet was redispersed in 10 mL of H_2O and filtered. For electron microscopy studies, the dispersion was diluted 10-fold and 10 μL were drop-casted on a carbon film coated copper grid (Electron Microscopy Sciences, 150 mesh) and dried under vacuum overnight at room temperature. This concentration was also used for optical absorption and photoluminescence studies.

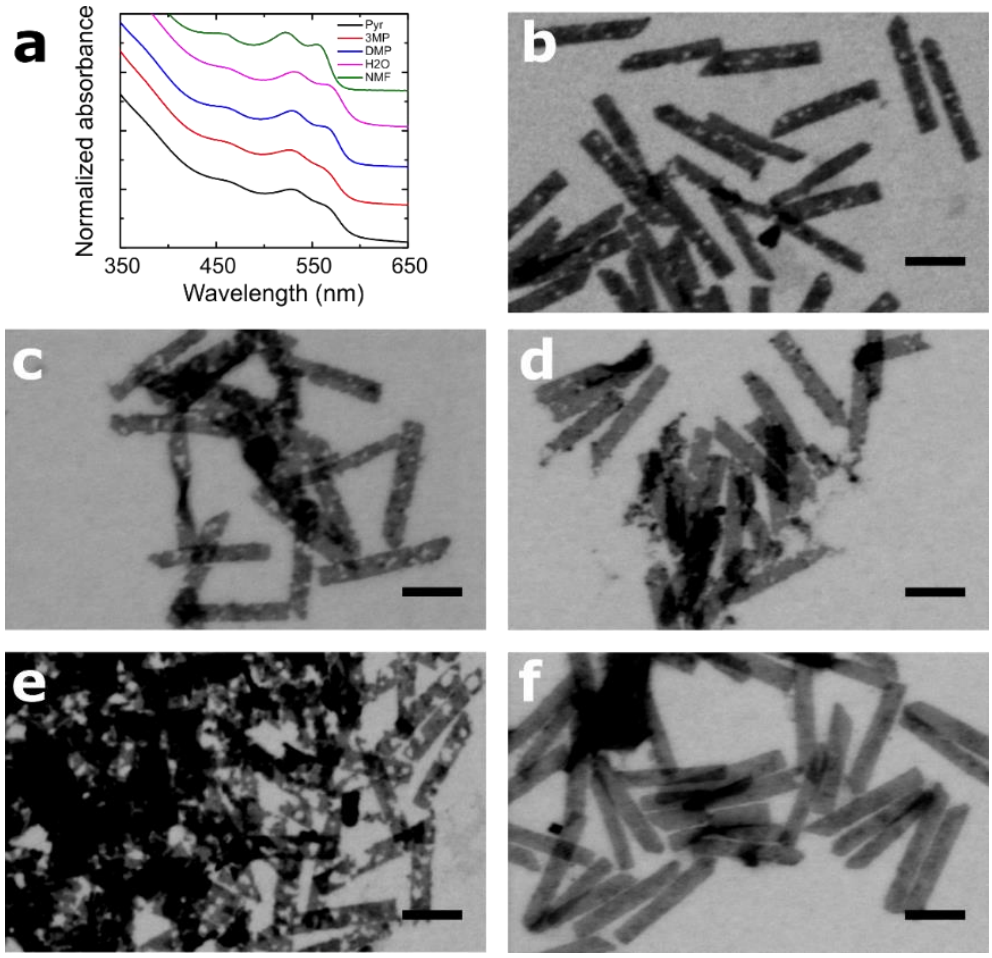

Figure S2 (a) Absorption spectra of NPs (reaction time: 30 minutes) in water after LE. The legend indicates the composition of the polar phase during LE. Bright field STEM images of NPs after LE; the composition of the polar phase during LE was (b) Pyr, (c) 3MP, (d) DMP, (e) H_2O, and (f) NMF. Scale bars indicate 50 nm.

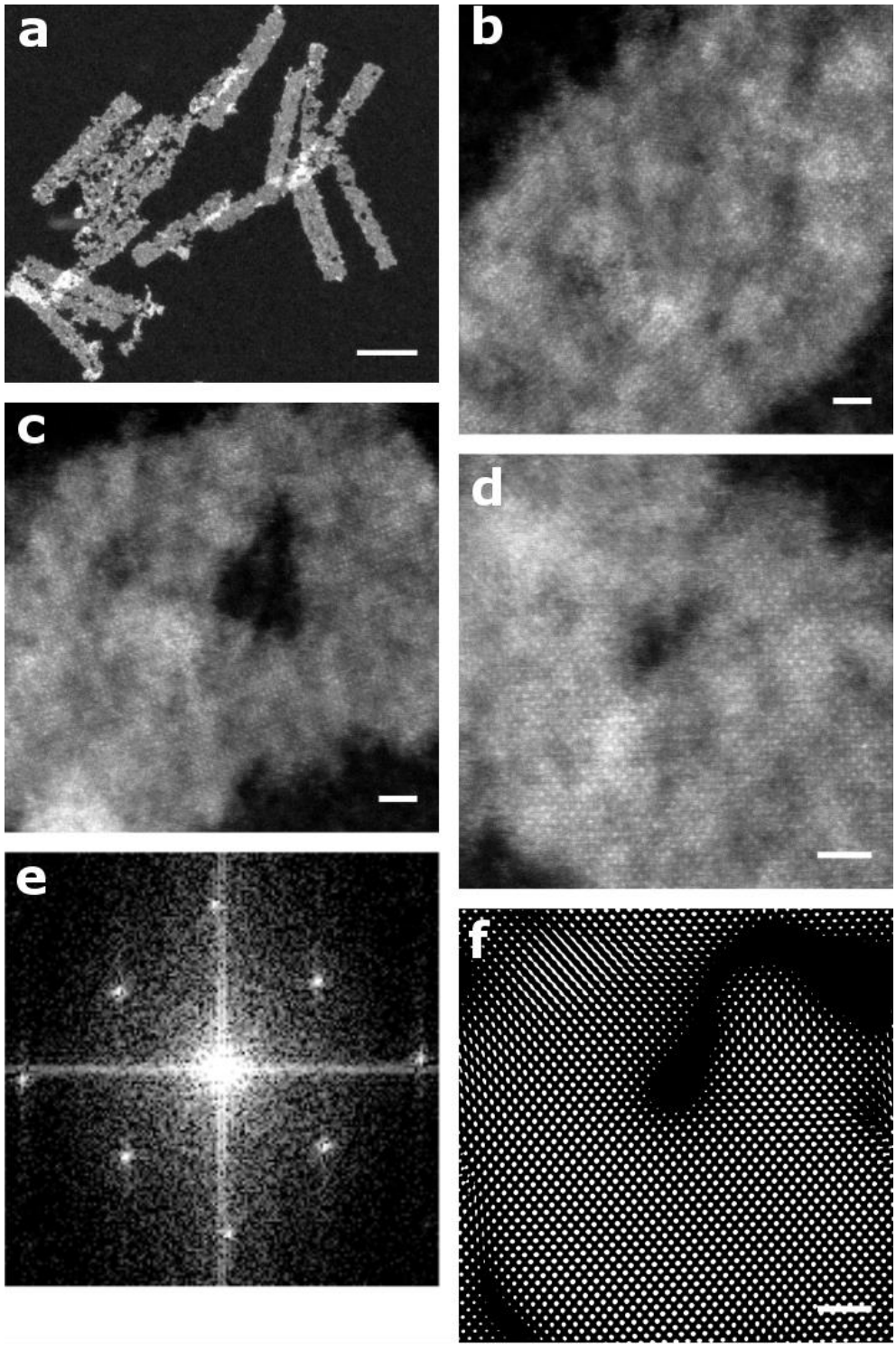

Figure S3 HAADF STEM images of damaged NPs (reaction time: 30 minutes) post LE for medium (a) and high (b-d) magnifications. Contrast variation along individual NPs is visible and can be interpreted as material deposition during LE (see main text). (e) Fast Fourier transform image of (d), showing the square atomic lattice features of NPs. (f) Inverse fast Fourier transform of (e) clearly showing the damage to the atomic lattice. Scale bars indicate 50 nm (a) and 2 nm (b-d,f).

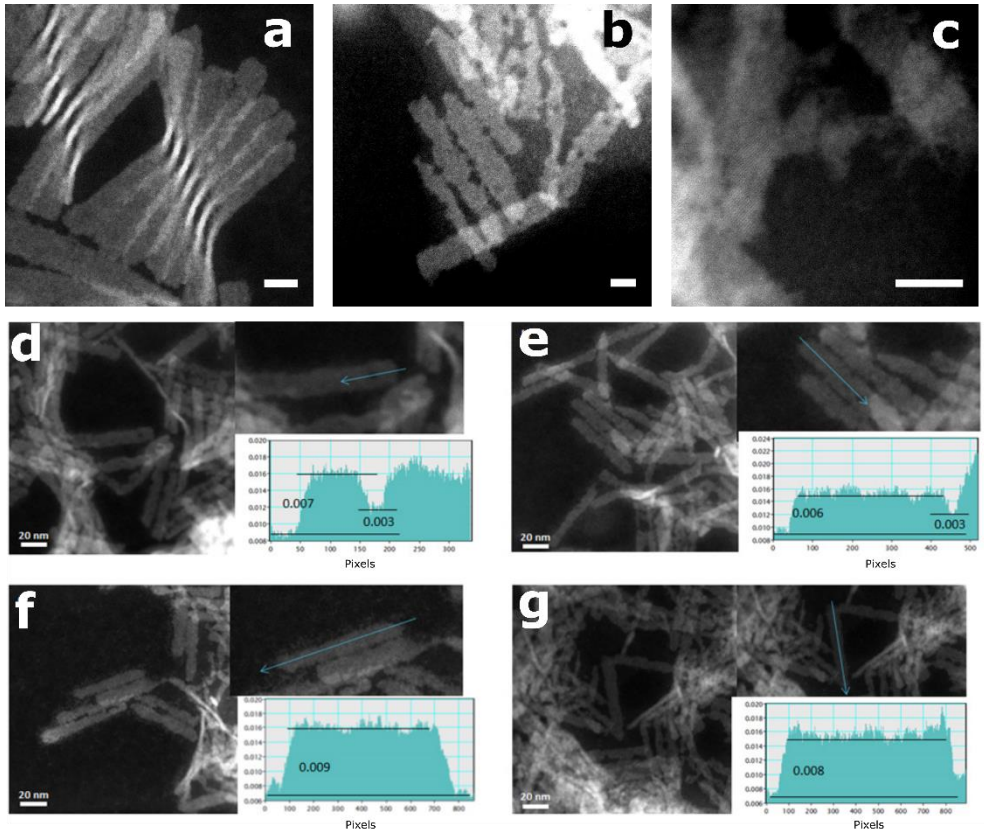

Figure S4 High resolution HAADF STEM images of NPs (reaction time: 20 minutes, see Figure S2). (a) Pristine NPs; (b) NPs after ligand exchange with $NH_4Sn_2S_6$ ligands; (c) NPs after recovery with 33% v/v solution of DMP in H2O. Scale bars indicate 10 nm. (d-g) Thickness measurements using calibrated intensities in HAADF STEM images of ligand-exchanged NPs in the presence of NH_4OH before (d,e) and after (f,g) recovery treatment with DMP. Each panel shows a zoomed-out image on the left, enlarged section with line scan (arrow) on the upper right, and the resulting measured thickness along this line scan on the lower right. Defective NPs (d,e) show a decrease of the thickness of at least 50% of the total thickness. These dips are absent in the recovered samples (f,g).

Measurement	After ligand exchange	After DMP healing	Relative change
1	0.0074	0.0076	/
2	0.0077	0.0075	/
3	0.0086	0.0074	/
4	0.0063	0.0086	/
5	0.0077	0.0088	/
6	0.0080	0.0098	/
7	0.0062	0.0079	/
8	0.0069	0.0073	/
9	0.0093	0.0078	/
10	0.0060	0.0063	/
Mean intensity	0.0074	0.0079	+7%
Relative standard deviation	14%	11%	-3%

Table S1 Calibrated intensity values for 10 NPs after ligand exchange, and 10 NPs after DMP treatment.

Surface recovery

Surface recovery procedure was performed by diluting the dispersion of ligand exchanged NPs in a mixture of H_2O and L-type ligand (Pyr, 3MP, DMP) so to obtain a 10-fold dilution of NPs (respect to the concentration post LE) in a mixture of 3-33% v/v L-type ligand in H_2O. For electron microscopy studies, 10 μL of this dispersion was drop-casted on a carbon film coated copper grid (EMS, 150 mesh) and dried under vacuum overnight at room temperature (Figure S5 a). This concentration was also used for optical absorption and photoluminescence studies. The PL QY data shown in Figure 3 d can directly relate to the underlying structural state of NPs. The LE induced perforations introduce deep trap states within the electronic energy structure as observed in PL, and leave the NP crystal lattice strained as reported directly with STEM, resulting in a higher energy structural configuration.[5] Hence, each NP may relax to a lower energy minimum represented by the unstrained, undamaged state. In figure S5 b, we report the influence of DMP recovery on NPs that were ligand exchanged using either NH_4OH aqueous solution (yielding visually damaged NPs, red dots) or NMF (yielding visually undamaged NPs, blue dots) as polar phase. The loss of PL QY after ligand exchange is more pronounced when using NH_4OH solution, however, both PL QY values are exceeding small (PL QY <0.01). After treatment with DMP, the extent of PL QY of visually damaged NPs (NH_4OH) recovers by a factor of ~400 while that of visually undamaged NPs (NMF) increases by a factor of ~30. Remarkably, both protocols yield visually undamaged NPs with comparable PL QY values. These results show that even visually undamaged NPs

using NMF as polar phase during LE can be repaired by adding DMP, suggesting the presence of defects too shallow to be observed under the electron microscope. Furthermore, the extent of recovery seems to be proportional to the extent of the damage present. A description of the observed recovery process begins by understanding LE chemistry: An SnS_4^{4-} anion binds to undercoordinated surface Cd^{2+} cations through $n \in [1,2,3]$ sulfurs, while the remaining 4-n unbound sulfurs provide colloidal stability through electrostatic repulsion.[6] In this scenario, the thiostannate complexes effectively behave as a mixture of X- and L-type ligands, passivating the surface with CdX_2 and CdL species. Upon addition of an excess L-type ligand, such as DMP, L-promoted Z-type and L-type LE can take place extracting Cd and Se complexes from the higher energy amorphous deposits on the periphery of each NP (Figures 1 c and S3). This mobilization of material triggers a reconstruction of the NP surface, delivering the Cd and Se species to damaged areas.

To further investigate the proposed recovery mechanism, we report FTIR absorption spectra in Figure S5 c, measured on drop-casted thin-films of NPs dried on a hot plate at 150 °C for 1 hour to remove excess solvent. For the pristine sample, the main contribution in the frequency range shown comes from -CH stretching modes (~ 2900 cm^{-1}), likely related to surface-bound oleate ligands. After ligand exchange, absorption from -CH stretching modes mostly disappears and is replaced by a broad-band absorption mode peaking around 3250 cm^{-1} which we attribute to -OH stretching originating from a water film spontaneously forming on the now hydrophilic LE NPs thin-film. After surface recovery with DMP treatment, we can observe both -OH and -CH stretching modes. Since

the films have been dried at 150 °C for 1 hour, we conclude that the contribution from -CH modes likely originates from surface-bound DMP molecules, that therefore could not be removed by evaporation. This confirms that L-type ligand DMP indeed plays a role in the recovery of structural and optical properties of LE NPs.

To provide an estimate of the total thickness variation of the CdSe NPs after ligand exchange and after treatment with DMP, we analyzed calibrated STEM images (Figure S4 d-g) and compared them with the results of image simulations. The STEM images were converted to an absolute intensity scale using a detector normalization, such that intensities in the image are a fraction of the total incident beam intensity.[7] Figure S4 d,e shows the distribution of the calibrated intensities along two line scans across a defective NP after ligand exchange. After background subtraction, the image shows an overall intensity of 0.006 and 0.007 and an intensity of 0.003 at the defect positions. After DMP treatment (Figure S4 f,g), the overall intensity (0.008 and 0.009) is slightly higher than after ligand exchange. The calibrated intensity measurements show, assuming a linear intensity/thickness correlation, a decrease of thickness at the defective positions of at least 50% of the total thickness. We have repeated the measurement for 10 NPs after ligand exchange and 10 NPs after DMP treatment. In the former case, the intensity values were measured at non-defective positions. The results are shown in Table S1. After ligand exchange, an increase in intensity on average of about 7% is recorded, as compared to NPs before the healing treatment. This increase likely relates to the DMP healing mechanism investigated in this manuscript, as well as additional ligands at the surface (Figure S5 c).

Also the relative standard deviation, a measure for the thickness polydispersity, decreased after the recovery treatment, in line with the somewhat sharper absorption peak measured for these recovered samples.

In order to compare absolute scale intensities, the calibrated images are also compared with the average intensity of a simulated cell using the QUEP code in MuSTEM[8] for a room temperature CdSe crystal, assuming an aberration corrected probe and an accelerating voltage of 200 kV. The calculated intensities are 0.00763, 0.01498, and 0.02253 for 1, 2, and 3 unit cells (i.e. 2, 4, and 6 atomic layers, respectively). Although a comparison of simulations and calibrated values (corresponding to CdSe NPs with 2 atomic layers thickness) shows an underestimation of the thickness value in comparison to 4.5 atomic layers (the sharp absorption transition at 514 nm), the simulation clearly show a linear intensity/thickness correlation and an absence of a distinct electron channeling effect. Therefore, the above thickness approximation is valid. The underestimation of the experimental values is due to the reduced detector efficiency of the real HAADF detector, while 100% detector efficiency was estimated for the simulation.

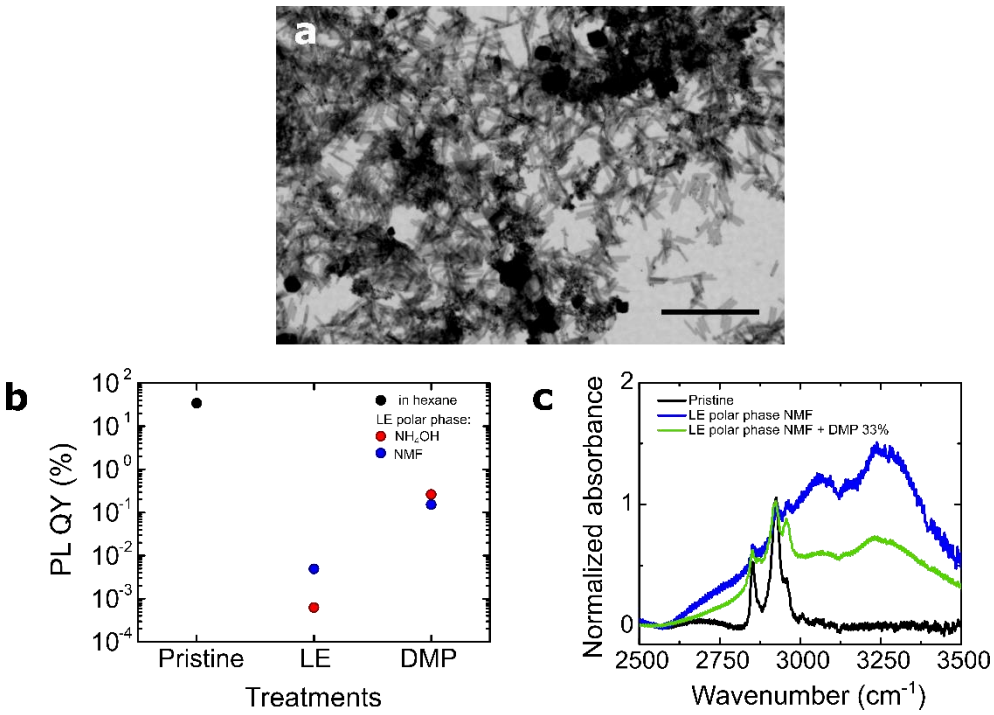

Figure S5 (a) Bright field STEM image of NPs (reaction time: 30 minutes) after surface recovery using 33% v/v DMP in H_2O. Scale bar indicates 500 nm. (b) Influence of DMP recovery route on PL QY of visually damaged (LE in presence of NH_4OH) and visually undamaged (LE in presence of NMF) NPs. (c) FTIR absorption spectra on drop-casted thin-films of NPs, after drying the solvent on a hot plate at 150 °C for 1h. For the sake of comparison between samples, absorbance was normalized to the value measured at 2926 cm^{-1} (position of one of the C-H stretching mode peaks).

Wet annealing (WA)

Wet annealing was performed by diluting the dispersion of ligand exchanged NPs in H_2O ten-fold; no DMP was used in this process. The dispersion was held at 100 °C while stirring for up to one hour. Aliquots were taken at regular intervals and quenched with the aid of an ice-bath to monitor the process with time. Short WA heals surface defects and greatly increases PL QY (Figure 3 b). For longer WA times, an interesting NP network is generated, over which the electron wavefunction is likely to be delocalized, whilst the holes may get trapped at the surface and specifically on dangling sulfur atoms (S6).[6] We also investigated the effect of WA on visually damaged (LE by using NH_4OH aqueous solution as polar phase) as well as undamaged (LE by using NMF as polar phase) NPs. It is apparent how the choice of polar phase for ligand exchange has a direct influence not only on the structural integrity of NPs but also on the sharpness of excitonic transitions in absorption spectra (Figure S6 c). The results on PL QY are shown in Figure S6 d. Performing WA treatment on visually damaged NPs yields the best results, although PL QY deteriorates faster with WA time than when using visually non-damaged NPs.

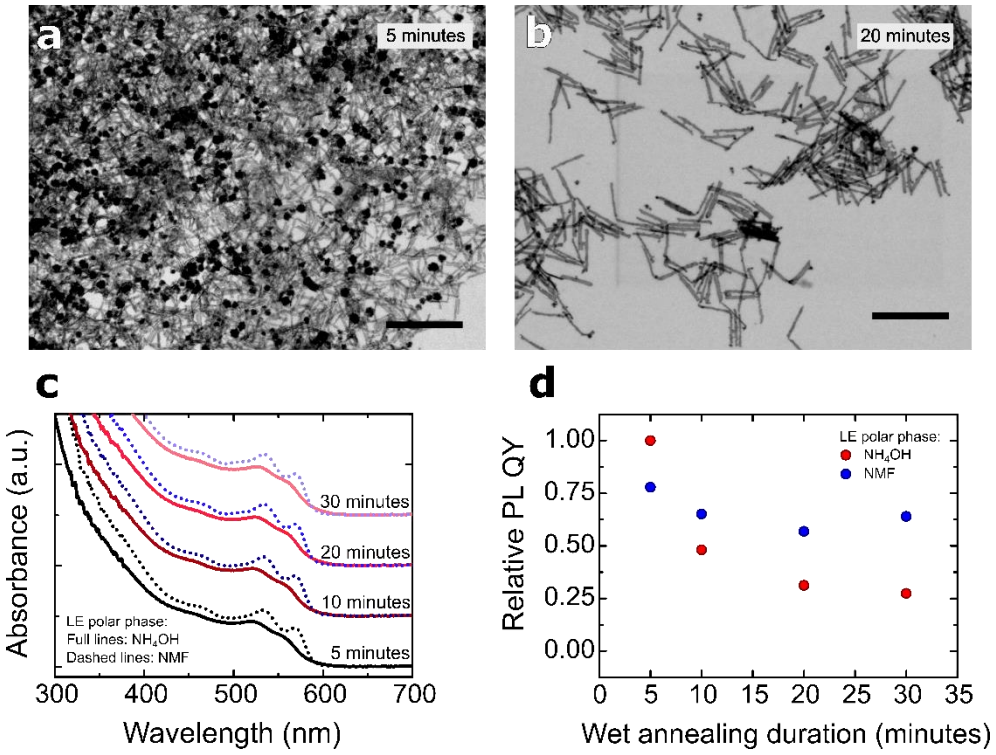

Figure S6 Bright field STEM image of NPs (reaction time: 30 minutes) after 5 minutes (a) and 20 minutes (b) of Wet Annealing treatment. Necking sites are clearly visible. The process does not significantly influence length and aspect ratio of the NPs (see Figure S7). Scale bar indicates 200 nm. Influence of Wet Annealing treatment on absorption spectra (c) and PL QY (d) of NPs ligand exchange using either NH_4OH aqueous solution or NMF as polar phase. Absorption spectra were shifted for clarity. PL QY was normalized to first time point.

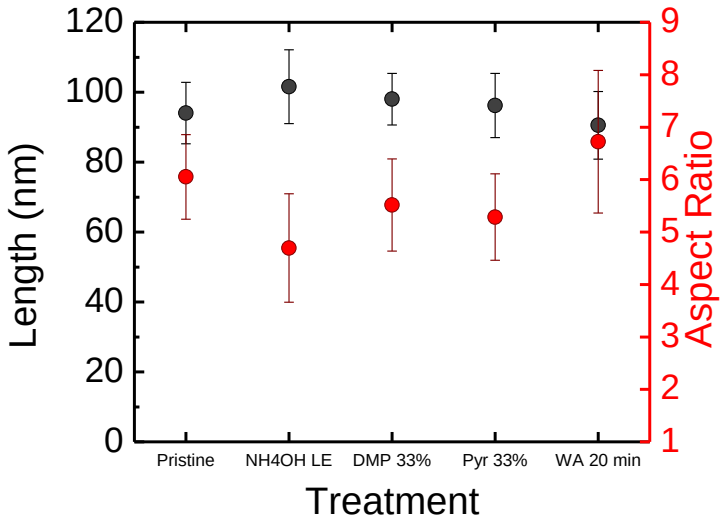

Figure S7 Measured length and aspect ratio (length/width) of pristine NPs (reaction time: 30 minutes) and after the treatments studied in this work (LE, recovery, WA) from STEM images. Percentages are referred to v/v. Error bars represent the standard deviation values obtained by a sample of > 100 NPs for each treatment in consideration.

Hydrodynamic radii of NPs measured with Dynamic Light Scattering

We have measured the hydrodynamic radii (R_H) of NPs in solution in the pristine state, after LE, and after surface recovery. The results are shown in Figure S8 (a-d). Scattered light intensity correlation curves $g_2(\tau)$ - 1 have been fitted to a single exponential of the type exp(-t/τ), where t is the delay time and $\tau^{-1} = (k_B T/6\pi\eta R_H)q^2$, the term in brackets being the diffusion coefficient (k_B is Boltzmann's constant, T the temperature, η the solvent's viscosity and q the wavevector). A single decay identifies a single population of diffusing objects, and therefore excludes the presence of aggregates. The only case where we have used a double exponential fit is DMP 33%; the faster component derives from the solvent density fluctuations present in a binary mixture of DMP and H_2O, and therefore unrelated to the diffusion of NPs.[9] To further study the presence of possible NP aggregates we fitted our data to a linear combination of exponential decays of the type $\int_{\tau_{min}}^{\tau_{max}} G(\tau)e^{-t/\tau}d\tau$. The distribution of the weights G plotted as a function of R_H yields the distribution function shown in Figure S8 (e-h). We note the values for average R_H agree quite well with the results of single exponential fits, the results of which are shown as text. The width of the distribution is constant for the different treatments, confirming the lack of aggregates in the system. However, the WA sample shows an asymmetric distribution of sizes with a prominent tail towards larger radii (Figure S8 h). This is consistent with our results from STEM which clearly show the NPs bridging and forming a network (Figure S6 b).

Finally, we have tested the colloidal stability of pristine NPs in solution in tetrahydrofuran (THF) during 24 hours (Figures S8 i,j). To perform the measurement, the stock dispersion was diluted 100-fold. Nanoplatelets appear fully dispersed: the hydrodynamic radius remains unchanged in time (Figure S8 i). As a further confirmation, the scattered light intensity also remains unaltered in time (Figure S8 j). The value of hydrodynamic radius we measure (~ 100 nm) is consistent with the measured length of NPs from STEM (95 nm).

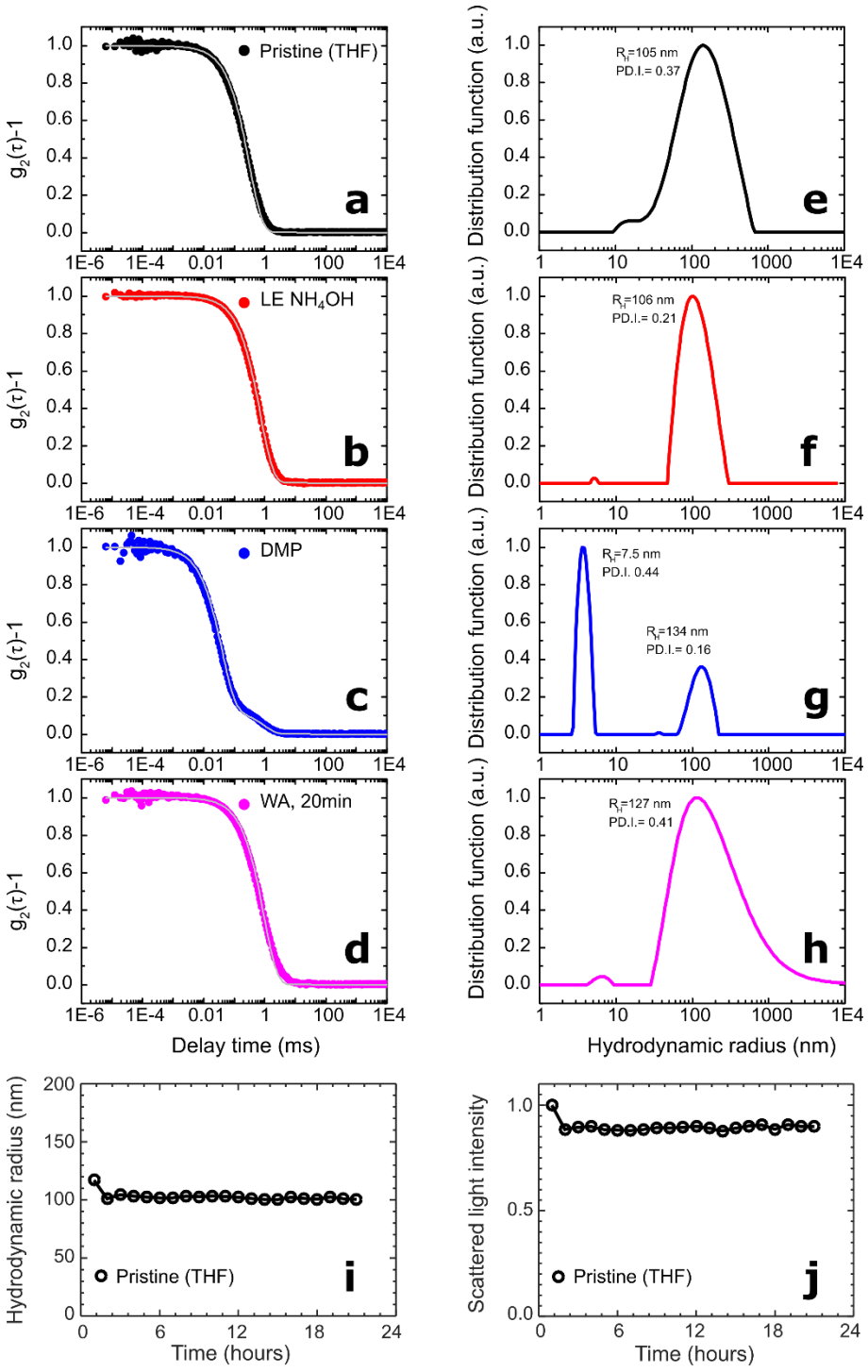

Figure S8 Scattered light intensity correlation curves from Dynamic Light Scattering on NPs (reaction time: 30 minutes) after performing the treatments described in this manuscript: pristine (a), LE in presence of NH_4OH (b), recovery with DMP (c) and with WA (d). Single exponential fitting show excellent agreement with data in a-d, while a double exponential fitting is shown in c. The distribution functions resulting from fitting the data with a linear combination of exponentials are shown in e-h. The fitting parameters shown in print refer to the single and double exponential fitting shown in a-d and show good agreement with the distribution function fitting approach. (i,j) Test of colloidal stability of pristine NPs dispersed in tetrahydrofuran. Average hydrodynamic radius (i) and scattered light intensity (j) versus time.

Time Resolved Microwave Conductivity of NPs thin films

We have measured the conductivity of films of NPs before and after LE with thiostannate complexes with the Time Resolved Microwave Conductivity (TRMC) technique. TRMC, is a contactless, pump-probe technique that measures the photoconductance of a thin-film and extrapolates a value for conductance at zero photon flux for very low values of incident laser power. The sample is optically excited at 500 nm with a pulsed Q-switched Nd:YAG laser inside of a resonant microwave cavity. The generation of charge carriers causes a loss in microwave power reflected by the cavity which is directly proportional to the photoconductance of the sample, and hence the mobility of charge carriers. Extrapolating the photoconductance of the sample for zero photon flux allows to obtain an estimate for the conductivity of the film in the absence of higher-order recombination events. Additionally, studying the kinetics of the recovery of the loss of reflected power by the cavity after the laser pulse gives insight on the kinetic processes at stake in charge carrier recombination. The mean path length of carriers in high-mobility TiO_2 thin films from Fravventura et al. was found to be 6.5 nm; adjusting for the difference in effective mass to CdSe we estimate the mean path length to be 28 nm.[10] Therefore, the volume probed with this technique is localized to a single nanoplatelet. We show the results for NPs before and after LE with thiostannate ligands in Figure S9. We notice how the decay time of the photoconductance signal shortens considerably in LE NPs (< 40 ns, Figure S9 b-d) compared to pristine NPs (~ 300 ns, Figure S9 a). This shows that in LE NPs charge trapping takes place much faster as a result of the formation of non-radiative

recombination channels (Figure S9 f). This result is consistent with the observation of surface degradation under STEM and PL QY decrease in LE samples. Furthermore, the extrapolated values for the conductivity of the different samples follow the same trend as the PL QY (Figure S9 e). This supports the idea that the volume of material probed with this technique is comparable to the size of a single NP (in plane dimensions 70 nm x 14 nm) and therefore the observed photoconductance should be regarded as an intrinsic property of an individual NP and not related to inter-NP charge transport. Consequently, the conductivity values of NPs extracted with TRMC represent a measure of the quality of the material (presence of traps) similarly to PL QY. TRMC results corroborate the analysis of material quality of NPs before and after LE with thiostannate complexes performed in this work based on optical and structural studies.

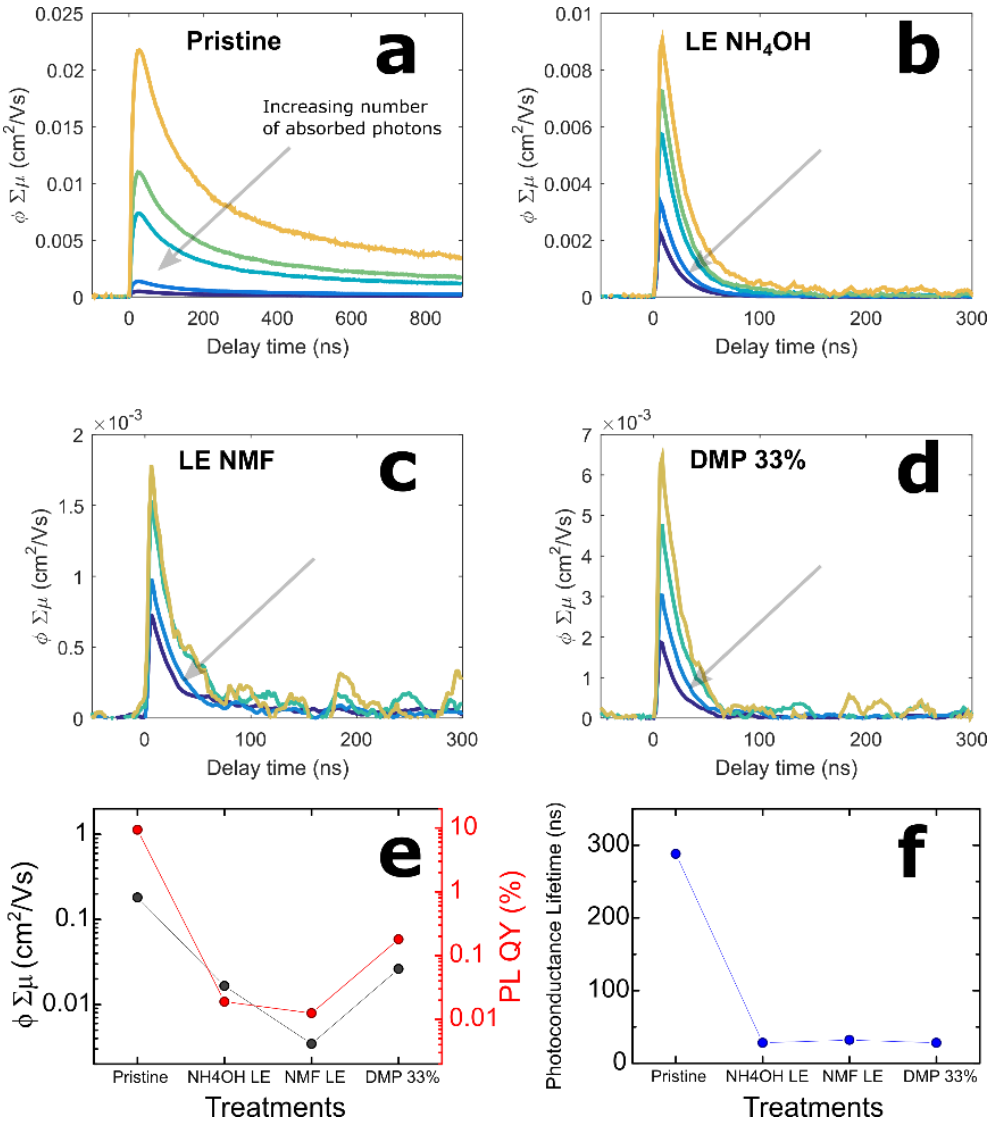

Figure S9 TRMC transients for increasing photon flux measured on NPs films after performing the treatments described in this manuscript: (a) Pristine, (b), after LE in presence of NH_4OH, (c) after LE in presence of NMF, (d) after recovery with DMP. The extrapolated values for the conductivity are shown in (e) and show good agreement with the PL QY results independently performed on dispersion of NPs. The photoconductance lifetimes for the lowest photon flux are shown in (f).

DC conductivity of NPs thin films

We have measured the DC conductivity of thin films of drop-casted NPs after the treatments considered in this work. The results are shown in Figure S10. Pristine NPs show a barely measurable response to the applied drain voltage (voltage applied between the source and drain contacts). Instead, NPs LE for thiostannate complexes show a considerable increase in drain current (current measured between source and drain contacts), with the sample LE in presence of NMF showing the best performance (Figure S10 a). For this sample we have measured the drain current – drain voltage curves for different gate voltages applied, and noticed the presence of hysteresis (Figure S10 b). Electrical hysteresis is commonly observed in nanoparticle devices and attributed to charge carrier trapping. Furthermore, we have extracted the electron mobility for the champion device from the slope of the drain current – gate voltage curve in the linear regime (Figure S10 c).[11] We estimate the value of the mobility to be $5 \cdot 10^{-4}$ cm^2/Vs. The influence on DC thin film conductivity of chemical and thermal recovery routes on ligand-exchanged NPs thin-films is shown in Figure S10 d for LE NPs in NH_4OH and Figure S10 e for LE NPs in NMF. Thermally treating (WA) each NP dispersion for 5 minutes induces an increase in conductance for NPs ligand-exchanged using either NH_4OH aqueous solution or NMF as polar phase. By contrast, the chemical recovery route yields an increase in conductance only for NPs LE in presence of NMF. It is possible that surface-bound DMP molecules limit the conductivity of structurally recovered samples (see Figure S5 c). In all cases, LE dramatically improves conductivity over pristine NPs while recovery improves perfor-

mance in some cases. A more detailed analysis of the electrical characteristics of thin films of NPs LE with conductive ligands will follow in a separate report.

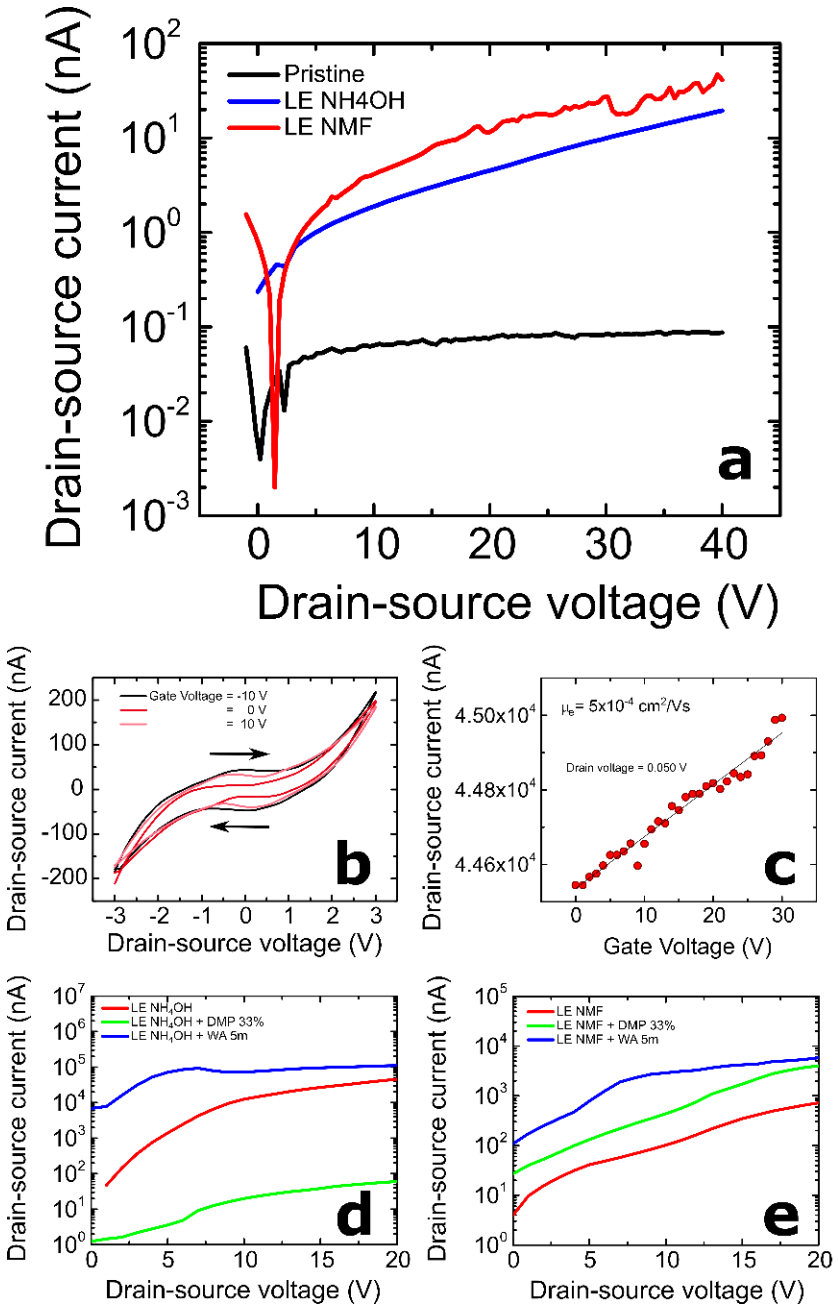

Figure S10 DC conductivity measurements on NP thin films for the various treatments investigated in this work. (a) Drain current as a function of drain voltage, for an applied gate voltage of 0 V, for NPs ligand-exchanged using either NH_4OH aqueous solution or NMF as polar phase. (b) Sweeps in drain current versus drain voltage for different gate voltages applied, measured on NPs ligand-exchanged using NMF as polar phase. (c) Drain current as a function of gate voltage for fixed drain voltage of 0.050 V, measured on NPs LE in presence of NMF (champion device). From the linear fitting shown we can estimate the value for the electron mobility. (d) Drain current as a function of drain voltage, for an

applied gate voltage of 0 V, for a drop-casted thin-film of NPs ligand-exchanged using NH_4OH aqueous solution as polar phase, and further processed following DMP or thermal treatment discussed in the text. (e) Drain current as a function of drain voltage, for an applied gate voltage of 0 V, for a drop-casted thin-film of NPs ligand-exchanged using NMF as polar phase, and further processed following DMP or thermal treatment discussed in the text.

Effect of LE, recovery and WA treatments on QDs

We have compared the effects of LE, recovery and WA treatments studied on NPs in the main text with QDs of diameter (~2.9 nm) comparable to the thickness of NPs. The QDs diameter has been deduced by the sizing curves provided in the literature, and specifically by the position of the first exciton peak (545 nm).[12] QDs were synthesized using a similar protocols as NPs and identical precursors.[2] The results are shown in Figure S11. Panel (a) and (b) show the absorption spectra of pristine QDs, as well as after LE, recovery and WA procedures. It is apparent how the changes are not as dramatic as observed with NPs. The shift of the first exciton peak from pristine to ligand exchanged QDs is about 15 nm, therefore much smaller respect to NPs (60 nm). Furthermore, while for QDs the shape of the absorption spectrum remains essentially unchanged, for NPs this is not the case as the excitonic features broaden after LE. It is interesting to notice how the shape of the absorption spectrum for ligand exchanged NPs is similar to that of CdSe/CdS core/shell NPs synthesized by another group.[13] It is therefore likely that the observed changes in the absorption features for NPs after LE are due to the surface passivation with tin-based (thiostannate) ligand that provides the NP with an CdS monolayer. The non-uniformity of passivation along the NP surface may also cause the broadening of the excitonic features. The absorption spectrum of QDs also changes during the WA process:

the first exciton peak gradually loses definition (total increase in FWHM of 17 nm) although the peak position does not shift. We can propose that the surface of QDs suffers mild rearrangement during WA (causing the increase in FWHM) while the particles do not seem to effectively grow. This is probably because one NP (lateral dimensions 95 nm x 15 nm) has roughly 130 times more surface area than a QD. Therefore: (1) Collisional cross section of NPs is higher than QDs; (2) Surface reconstruction is likely to be more favourable in NPs than in QDs. Photoluminescence quantum yield (QY) results (panel c) support this interpretation. While surface reconstruction via chemical route gives similar results for QDs as for NPs, taking the thermal route actually decreases the QY. In this case, the higher temperature may actually favour desorption of surface passivating ligands and therefore introduce new surface defects.

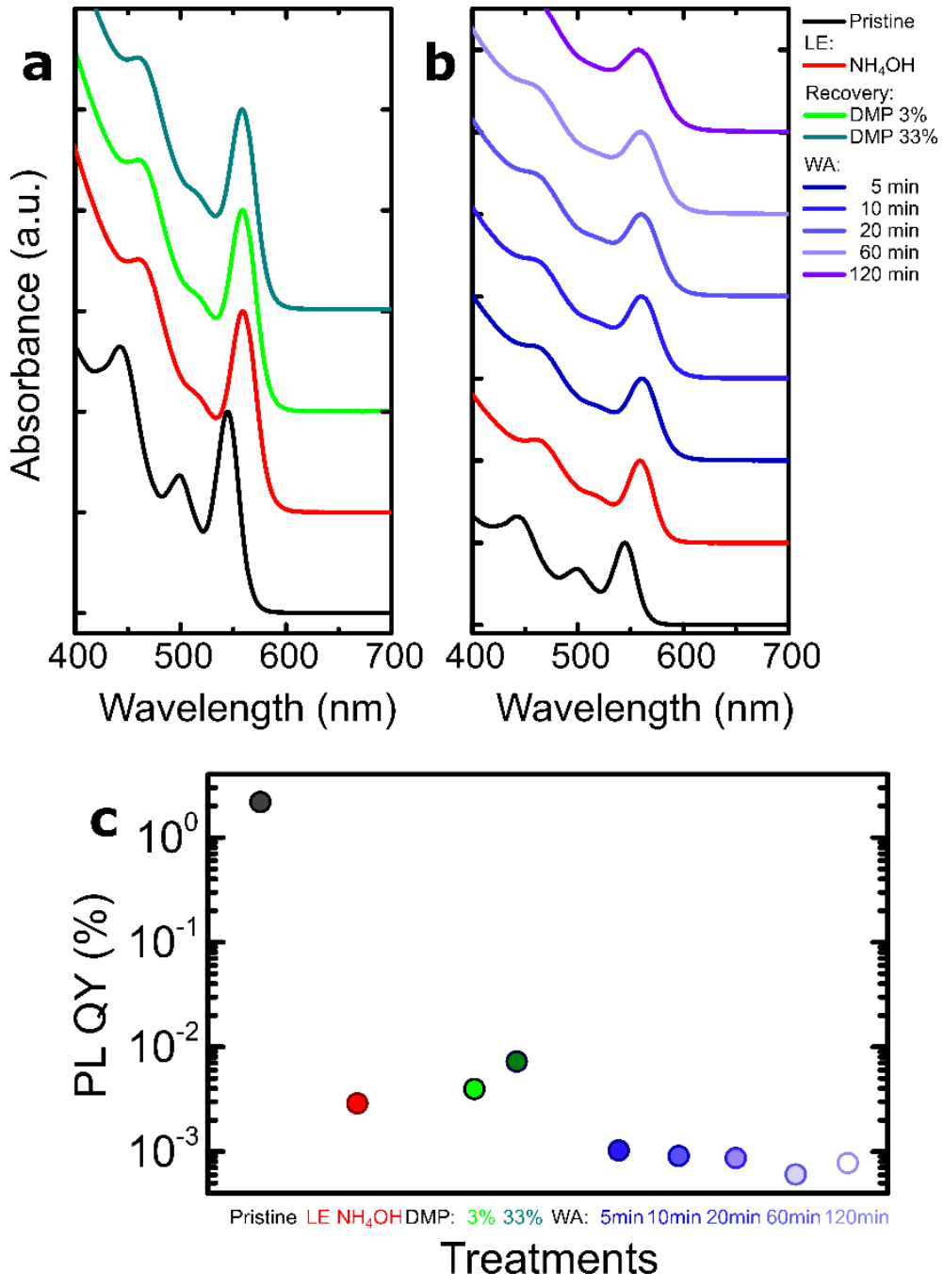

Figure S11 Spectroscopic properties of CdSe quantum dots exposed to surface treatments studied in this work. (a) Absorption spectra of quantum dots before LE, after NH_4OH-based LE, and after recovery with 3% and 33% v/v DMP in H_2O. (b) Absorption spectra of quantum dots during WA treatment, as compared to pristine and post-LE conditions. (c) PL QY of band-edge emission from quantum dots for all the considered treatments.

Characterization methods:

Scanning Transmission Electron Microscopy (STEM) and image analysis

For low and medium magnification STEM studies we used a Verios XHR SEM (FEI). The microscope was operated at 20 kV and 100pA in transmission mode using a STEM detector. Bright field and high angle annular dark field (HAADF) images were simultaneously recorded. High resolution STEM was performed using a FEI Titan 80-200 ("ChemiSTEM")[14] electron microscope operated at 80 kV, equipped with a spherical-aberration (Cs) probe corrector (CEOS GmbH), and a HAADF detector. We analyzed the STEM images by using ImageJ software to adjust the contrast, measure the size of NPs, perform fast fourier transform (FFT) algorithm to study the crystalline structure of NPs and inverse FFT to study the damaged areas from the LE procedure. Results shown concerning lateral dimensions of NPs represent the average over >100 NPs.

Optical absorption measurements

Optical absorption spectra in the visible/near infrared range were measured using a Perkin Elmer Lambda 950 UV/Vis/NIR spectrophotometer. The concentration of NPs and QDs was chosen so that the value of absorbance at the first exciton peak would not exceed 0.1. Typical dilution factors used range from 100 to 500 compared to stock dispersions.

Absorption spectra in the infrared were measured using Bruker VERTEX 70/70v FTIR spectrometer. NPs dispersions were dropcasted on double-side polished silicon wafer that

had been cut and piranha-cleaned. To aid solvent evaporation, substrates were placed on a hotplate at 150 °C for 1 hour.

Photoluminescence measurements and fitting routine

Photoluminescence spectra were measured using a Horiba Fluorolog-3 spectrofluorometer. Photoluminescence spectra were converted to energy space prior to fitting following literature.[15] The fitting routine involved: (1) fitting the low energy defect band with a Gaussian; (2) subtracting the resulting Gaussian fit from the complete experimental curve; (3) fitting the higher energy band-edge emission curve with a Lorentzian (pristine) or Gaussian profile (LE, recovery, WA). Photoluminescence QY was calculated relatively to a solution of Rhodamine 6G in Ethanol following literature, and namely correcting for using different integration times, band pass filters and percentage of absorbed light at the excitation wavelength (400 nm).[16]

Dynamic Light Scattering

We use an ALV DLS setup featuring a digital correlator and a 633 nm HeNe laser (35 mW) to minimize fluorescence. A typical DLS run was 180 s long and the measurement took place at 20 °C. Scattered photons reaching the two photodetectors were cross-correlated to give one intensity correlation function per measurement. The curves were fitted to a single or double exponential decay using Matlab, or to a linear combination of exponential using ALV proprietary fitting routine ("regularized fit").

Time-resolved Microwave Conductivity

The samples' photoconductivity was measured using the time-resolved microwave conductivity (TRMC) technique. A detailed description of the technique and methods can be found elsewhere.[17] Briefly, samples were drop casted on 1 mm thick quartz substrates, placed in a microwave cavity driven at 8.5 GHz, and illuminated at a wavelength of 500 nm, 3 ns pulsed Nd:YAG laser at a 10 Hz repetition rate. The change in microwave power is measured and averaged over 1-10 minutes depending on the photon flux. The photon flux is reduced with a series of neutral density filters (increasing the averaging time with decreasing photon flux) from 10^{15} to 10^{13} cm^{-2} to determine where higher order recombination processes no longer dominate the signal decay. The mobility values reported here are given at a photon flux where the mobility is independent of flux (~ 10^{14} cm^{-2}).

DC conductivity

We have employed commercially available FET structures (Fraunhofer) in bottom gate configuration with a channel width of 10 mm and lengths ranging from 2.5 – 20 μm. Prior to samples deposition, the substrates were sonicated in acetone and 2-propanol (10 minutes each), and dried under a stream of dry nitrogen. NPs dispersions were dropcasted after being diluted respect to the stock solution by a factor of 1-10. Substrates were dried under vacuum to remove excess solvent. Electrical measurements have been obtained with a Keysight B2901A Source/Measure unit.

Supporting references

[1] a) M. V. Kovalenko, M. I. Bodnarchuk, J. Zaumseil, J. S. Lee, D. V. Talapin, *J Am Chem Soc* **2010**, *132*, 10085-10092; b) B. Krebs, S. Pohl, W. Schiwy, *Zeitschrift für anorganische und allgemeine Chemie* **1972**, *393*, 241-252; c) v. W. Schiwy, S. Pohl, B. Krebs, *Zeitschrift für anorganische und allgemeine Chemie* **1973**, *402*, 77-86.

[2] O. Carion, B. Mahler, T. Pons, B. Dubertret, *Nature protocols* **2007**, *2*, 2383-2390.

[3] C. X. She, I. Fedin, D. S. Dolzhnikov, P. D. Dahlberg, G. S. Engel, R. D. Schaller, D. V. Talapin, *Acs Nano* **2015**, *9*, 9475-9485.

[4] M. V. Kovalenko, M. Scheele, D. V. Talapin, *Science* **2009**, *324*, 1417-1420.

[5] A. Riedinger, F. D. Ott, A. Mule, S. Mazzotti, P. N. Knüsel, S. J. Kress, F. Prins, S. C. Erwin, D. J. Norris, *Nat Mater* **2017**.

[6] L. Protesescu, M. Nachtegaal, O. Voznyy, O. Borovinskaya, A. J. Rossini, L. Emsley, C. Coperet, D. Gunther, E. H. Sargent, M. V. Kovalenko, *J Am Chem Soc* **2015**, *137*, 1862-1874.

[7] a) J. M. LeBeau, S. Stemmer, *Ultramicroscopy* **2008**, *108*, 1653-1658; b) K. MacArthur, T. Pennycook, E. Okunishi, A. D'Alfonso, N. Lugg, L. Allen, P. Nellist, *Ultramicroscopy* **2013**, *133*, 109-119; c) A. Rosenauer, K. Gries, K. Müller, M. Schowalter, A. Pretorius, A. Avramescu, K. Engl, S. Lutgen, in *Journal of Physics: Conference Series, Vol. 209*, IOP Publishing, **2010**, p. 012009.

[8] B. Forbes, A. Martin, S. Findlay, A. D'alfonso, L. Allen, *Phys Rev B* **2010**, *82*, 104103.

[9] J. Cox, *Journal of the Chemical Society (Resumed)* **1952**, 4606-4608.

[10] M. C. Fravventura, D. Deligiannis, J. M. Schins, L. D. Siebbeles, T. J. Savenije, *The Journal of Physical Chemistry C* **2013**, *117*, 8032-8040.

[11] D. M. Balazs, D. N. Dirin, H.-H. Fang, L. Protesescu, G. H. ten Brink, B. J. Kooi, M. V. Kovalenko, M. A. Loi, *Acs Nano* **2015**, *9*, 11951-11959.

[12] W. W. Yu, L. Qu, W. Guo, X. Peng, *Chem Mater* **2003**, *15*, 2854-2860.

[13] B. Mahler, B. Nadal, C. Bouet, G. Patriarche, B. Dubertret, *J Am Chem Soc* **2012**, *134*, 18591-18598.

[14] A. Kovács, R. Schierholz, K. Tillmann, *Journal of large-scale research facilities JLSRF* **2016**, *2*, 43.

[15] J. Valenta, *Luminescence Spectroscopy of Semiconductors*, Oxford University Press USA., **2012**.

[16] C. Würth, M. Grabolle, J. Pauli, M. Spieles, U. Resch-Genger, *Nature protocols* **2013**, *8*, 1535-1550.

[17] a) T. J. Savenije, A. J. Ferguson, N. Kopidakis, G. Rumbles, *The Journal of Physical Chemistry C* **2013**, *117*, 24085-24103; b) R. W. Crisp, R. Callahan, O. G. Reid, D. S. Dolzhnikov, D. V. Talapin, G. Rumbles, J. M. Luther, N. Kopidakis, *The journal of physical chemistry letters* **2015**, *6*, 4815-4821; c) J. M. Schins, E. Talgorn, *Review of Scientific Instruments* **2011**, *82*, 064703.